Preprint Title	Stability and activity of platinum nanoparticles in the oxygen electroreduction reaction: is size or ordering of primary importance?
Authors	Kirill O. Paperzh, Anastasia A. Alekseenko, Olga A. Safronenko, Vadim A. Volochaev, Ilia V. Pankov and Vladimir E. Guterman
Publication Date	22 März 2021
Article Type	Full Research Paper
Supporting Information File 1	Supporting Information.docx; 639.5 KB
ORCID® iDs	Kirill O. Paperzh - https://orcid.org/0000-0003-4878-9728; Anastasia A. Alekseenko - https://orcid.org/0000-0001-7948-0948; Olga A. Safronenko - https://orcid.org/0000-0003-2466-6651; Ilia V. Pankov - https://orcid.org/0000-0001-5302-4792; Vladimir E. Guterman - https://orcid.org/0000-0003-0403-0074

Stability and activity of platinum nanoparticles in the oxygen electroreduction reaction: is size or ordering of primary importance?

Kirill O. Paperzh, Anastasia A. Alekseenko, Olga A. Safronenko, Vadim A. Volochaev, Pankov I.V., Vladimir E. Guterman*

Faculty of Chemistry, Southern Federal University, str. Zorge 7, Rostov-on-Don, 344090, Russia

Vladimir E. Guterman - gut57@mail.ru, guter@sfedu.ru

Abstract

Platinum-carbon catalysts are widely used in manufacturing proton-exchange membrane fuel cells. Increasing Pt/C activity and stability is an urgent task, optimization of their structure seems to be one of the possible solutions. In the present paper, Pt/C electrocatalysts which contained small (2 - 2.6 nm) nanoparticles of a similar size, uniformly distributed over the surface of a carbon support, were obtained by the original method of liquid-phase synthesis. A comparative study of the structural characteristics, catalytic activity in the oxygen electroreduction reaction and durability of the synthesized catalysts, as well as their commercial analogs has been carried out. It was shown that the ordering of the structural and morphological characteristics of Pt/C catalysts makes it possible to reduce the negative effect of NPs small size on their stability. As a result, the obtained catalysts are significantly superior to their commercial analogs in ORR activity, but not inferior to them in terms of stability.

Keywords Electrocatalyst, Morphology Control, Oxygen reduction reaction, Platinum Nanoparticles, Size Distribution

Introduction

Nowadays low-temperature proton exchange membrane (PEMFC) fuel cells are gaining wider application. This is due to their environmental friendliness, low operating temperature, high

adaptability of specific characteristics [1–3]. The key components of PEMFC membrane-electrode assemblies (MEA) are the proton-exchange polymer membrane and porous electrode layers, in which current-forming reactions of oxygen electroreduction (ORR) and hydrogen oxidation or an organic reducing agent oxidation, e.g. methanol, occur [4, 5]. The need in carrying out high rate electrode reactions requires electrocatalysts, platinum nanoparticles or its alloys (NPs), deposited mainly on nano/microparticles of carbon supports being the best choice [6–8]. The most important functional characteristics of the catalytic layers are their activity in the corresponding reactions and stability, which reflects the ability to maintain its activity during operation. These characteristics depend on the PEMFC operating conditions, the composition and structure of the catalytic layers, and the catalysts themselves [9].

Platinum-carbon catalysts, whose composition and structure determine their functional characteristics, make up the key component of MEA catalytic layers. Of particular importance is the study of the catalyst electrochemical behavior in the ORR, since it is at the cathode that strong polarization and pronounced degradation of the catalyst take place. Such a degradation occurs as a result of both the operation at high anodic potentials and the effect of aggressive oxygen-containing intermediates, which are formed during the multistage oxygen electroreduction reaction. When comparing platinum catalysts based on the same carbon support, differences in their electrochemical behavior are determined by the difference in the composition (Pt-loading in Pt/C), structure (shape and size of the platinum NPs, dispersion of their size and features of spatial distributions, and the strength of NPs adhesion to the support [10]. The latter is likely to depend on the method/conditions of the synthesis [11].

The number of publications related to the effect of the Pt/C catalysts structure on their activity, primarily in ORR, is rather large. Nevertheless, more and more new papers, specifying the peculiarities of such an influence, are being published every year. Initially, most researchers were inclined to believe that a decrease in the size of nanoparticles is accompanied by a significant decrease in the platinum specific surface activity. K. Kinoshita was one of the first to obtain such results [12]. As a first approximation, specific activity of platinum in the catalyst, being referred to the unit mass of the metal

I_{mass} (mass activity), is determined as a product of the electrochemically active surface area (ESA) multiplied by the specific activity (I_{sp}) of platinum:

$$I_{mass} = ESA * I_{sp} \quad (1).$$

It was found that with the increase in the ESA, the ORR mass activity of Pt/C passed through a flat maximum in the ESA values range of 60–90 m^2 g^{-1}(Pt), which was explained by the inverse dependence of each factor in formula (1) on the size of platinum NPs [13]. Later it was shown that the effect of the platinum NPs size on the specific surface activity was much weaker than it seemed to be at first. For example, according to the results [14], with a decrease in the average size of platinum nanoparticles from 5-6 nm to 1-2 nm, the specific ORR activity of Pt/C decreased no more than 2 times. In this case, an increase in ESA due to a decrease in the NPs size can prevail over a decrease in I_{sp} and, according to Eq. (1), leads to an increase in the mass activity of Pt/C catalysts containing ultra-small platinum NPs. For example, in [15, 16] the authors succeeded in obtaining Pt/C electrocatalysts based on ultra-small platinum NPs, which demonstrate a higher ORR mass activity in comparison with widespread commercial Pt/C analogs. In fact, different sites of NPs surface have different specific activities in the ORR [17], as a result the control of the NP shape, leading to an increase in the proportion of more active areas, can lead to a significant increase in the Pt/C activity [18]. Moreover, according to the calculations in [19], NP of each size can have its own optimal shape, which provides the highest ORR mass activity. Nevertheless, it is important to take into account that real Pt/C catalysts contain nanoparticles of different sizes. Control over the size of the particles can cause the change in their shape, which, in turn, can result in the formation of maximum on the curves of activity dependence on the average NPs size [20].

The effect of Pt/C catalysts structure on durability has been less studied than the effect on ORR activity. To assess the catalysts stability, one requires much longer testing than to evaluate their activity. Moreover, the correlation between the results of evaluating catalysts durability obtained during accelerated stress testing and the use of fuel cells in real practice is far from being perfect. Therefore, along with the study of the certain factors influence on the catalyst stability, the search for the optimal methods and conditions for stress testing in an electrochemical cell is still progress.

Degradation of electrocatalysts is a highly complex process and it can proceed in accordance with different mechanisms [9]. It has been established that the regression of the Pt/C functional characteristics can be associated with different reasons: dissolution of small platinum nanoparticles (less than 3 nm in size) [14, 21]; reprecipitation of platinum from small nanoparticles into larger ones [14, 22, 23]; agglomeration of nanoparticles in the process of their surface diffusion [9, 23]; a change in the shape of the nanoparticles [4, 24]. It can be due to the oxidation of the carbon carrier, which causes the detachment of platinum nanoparticles and the loss of their contact with the support [25, 26, 27], as well as the isolation of particles by adsorbed carbon monoxide released due to carbon oxidation [28–31]. Each of the mechanisms described above can play a greater or smaller role, depending on the conditions of the catalysts testing, the features of their composition and structure [32].

When the same support is used, the stability of Pt/C catalysts during their operation is affected primarily by the mass fraction of the metal and the size of the nanoparticles [33, 34]. Catalysts stability, as a rule, increases with increasing NPs size [14, 33–38]. The probability of agglomeration and coalescence of NPs during stress testing also decreases with an increase in the average distance between platinum NPs in catalysts, an increase in their stability being the result [14]. Apparently, a relatively high stability of the small-sized systems is possible when the platinum NPs are close in size and their distribution is uniform over the surface of the carbon support [36, 39–42]. For example, as it is shown in [42], the growth of the nanoparticles during the catalyst operation accelerates when large and small NPs are localized in the same regions of the support surface, and it slows down if the catalytic layer is formed from an ordinary mixture of two catalysts with small and large nanoparticles, respectively.

The need to reduce the content of expensive platinum in the catalysts, forces researchers to follow the path of reducing the size of NPs. However, the opposite effect of the NP size on the mass activity and stability of the catalysts, forces us to seek a compromise or, in other words, to seek structures with an optimal combination of the catalyst activity and stability. In this regard, of particular interest are the methods for the synthesis of catalysts, which make it possible to obtain materials that combine small size of the nanoparticles, their narrow dimensional and ordered spatial distribution over the surface and pores of support.

This study is based on the hypothesis that Pt/C catalysts containing small nanoparticles which are close in size, uniformly distributed over the surface of a carbon support, can be both more active and more stable than catalysts based on larger particles, but with less uniformity of dimensional and spatial distribution.

Thus, the aim of this study was to obtain Pt/C catalysts containing small NPs narrow in size and with uniform spatial distributions and to compare the ORR activity and stability of the obtained catalysts and conventional analogs containing NPs of a larger size, but with the less ordered dimensionally-structural characteristics. Taking into account the above requirement, we have chosen commercial catalysts that are widely used both in research and in fuel cells manufacture.

Results and Discussion

The X-ray diffraction patterns of the catalysts that we have synthesized, and the commercial analogs with different platinum contents have a similar shape, typical for Pt/C materials (Fig. 1). The presence of the nanosized platinum crystallites causes broadening of the characteristic maxima of platinum. The broadening increases with a decrease in the D_{Av}. The results of calculating the D_{Av} values according to the Scherrer equation are shown in Table 1.

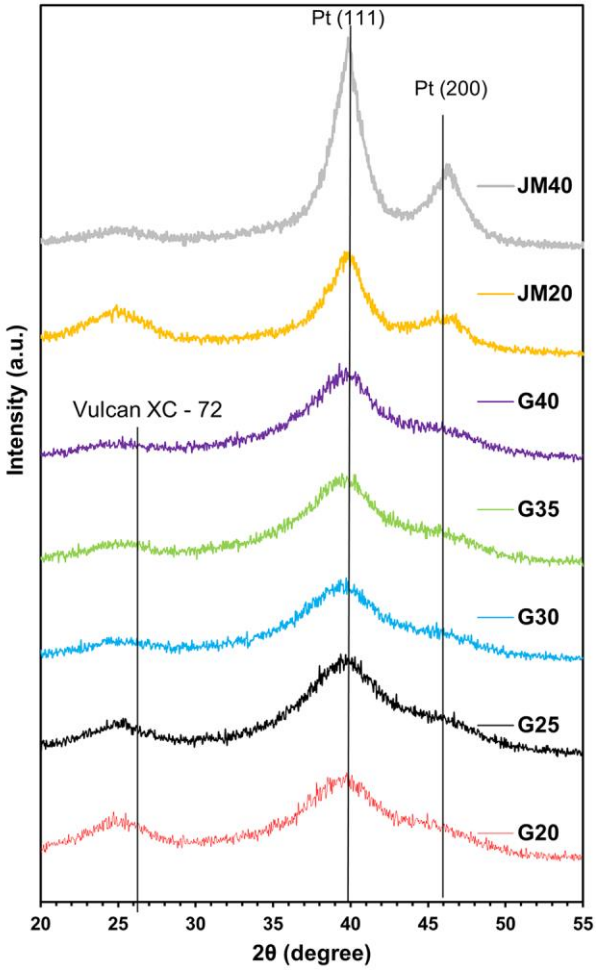

Figure 1: X-ray diffraction patterns of Pt/C materials.

Table 1: Parameters characterizing the composition and structure of Pt/C catalysts

Sample	Pt-loading in Pt/C, ω(Pt), wt. %		Average crystallites diameter, D_{Av}, nm (XRD)	Average NPs size, D_{NP}, nm (TEM)	Specific number of NPs, N, 10^{15} m^{-2}	Average distance between NPs, λ, nm
	Theoretical	Actual				
G_{20}	20	20.4 ± 0.6	1.2	2.0	9.6	8.0
G_{25}	25	24.7 ± 0.7	1.2	-	-	-
G_{30}	30	30.9 ± 0.9	1.3	2.6	9.8	7.4
G_{35}	35	34.0 ± 1.0	1.3	-	-	-
G_{40}	40	39.0 ± 1.2	1.3	2.6	13.0	6.2
JM_{20}	-	20.0 ± 0.6	2.5	2.7	4.5	12.2
JM_{40}	-	40.0 ± 1.2	3.7	3.7	7.6	9.9

The mass fraction of platinum in the obtained materials ranged from 20.4 wt. % (G20) to 39 wt.% (G40). The average crystallite size in the catalysts was from 1.2 nm (samples G20, G25) to 1.3 nm (G30, G35, G40) (Table 2). Selective electron microscopic study of the synthesized materials (Fig. 2) showed that with an increase in the Pt-loading in the catalysts, the average nanoparticle size also increased from 2 nm (G20) to 2.6 nm (G30, G40).

The difference in the sizes of nanoparticles (crystallites) determined from the results of X-ray diffractometry and TEM is typical for nanostructured Pt/C materials. It is due to several factors: the difference in the principles of calculation which serve the basis for the corresponding methods of research [43], the possible contribution of NPs structural defects to the broadening of the X-ray diffraction patterns maxima [44], and problems of ultra-small particles recognition in TEM micrographs. In the commercial catalysts JM20 and JM40, their composition being similar to that of G20 and G40, the average crystallite size is 2.5 and 3.7 nm, and the average NP size is 2.7 and 3.7 nm, respectively. Comparison of the NPs size distribution histograms indicates that in the synthesized Pt/C catalysts the smaller size of NPs is combined with their size distribution, which is narrower than that in commercial reference samples (Fig. 2). For example, in sample G20, 92% of NPs have the size of 2.0 ± 0.5 nm, while in the commercial analog JM20 they have the size of 2.75 ± 0.75 nm (Fig. 3). A similar difference is observed when we compared G40 and JM40 analog (Fig. 2).

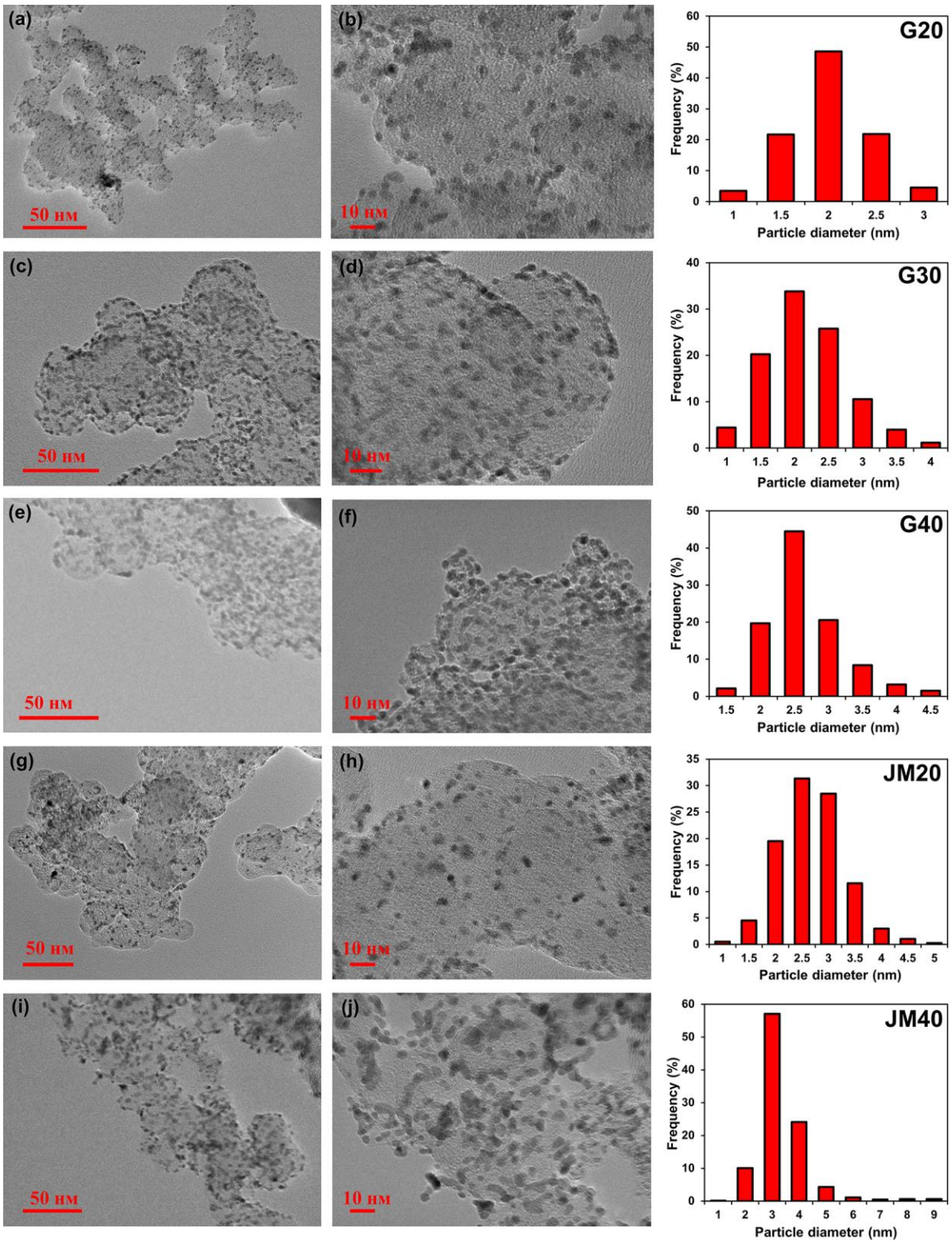

Figure 2: Micrographs of Pt/C samples of catalysts G20 (a, b), G30 (c, d), G40 (e, f), JM20 (g, h) and JM40 (i, j) and histograms of the nanoparticles size distribution in the corresponding materials.

We estimated the ordering of the spatial NPs distribution over the support surface. To this end, for each Pt/M material in TEM micrographs, we calculated the fraction of NPs not being in contact

(non overlapping) with other NPs or being in contact with one, two, or three other NPs. In this case, with the assumption that the smaller the number of intersections of NP images in the micrographs is, the more ordered NPs are distributed over the carrier surface. Disadvantages of such a simplified system used for analyzing the distribution uniformity are due to the following reasons: i) need to analyze the structure of a three-dimensional object from its two-dimensional image, and ii) consideration of intersections, in the case when NPs are located on the lower and upper parts of the carbon particle but only their images overlap. Nevertheless, even such a comparison proves to be useful, especially in the case of comparing Pt/C materials with a similar specific number of nanoparticles per unit of surface. The histograms of the NPs distribution by the number of intersections for different samples are shown in Fig. 3a-e.

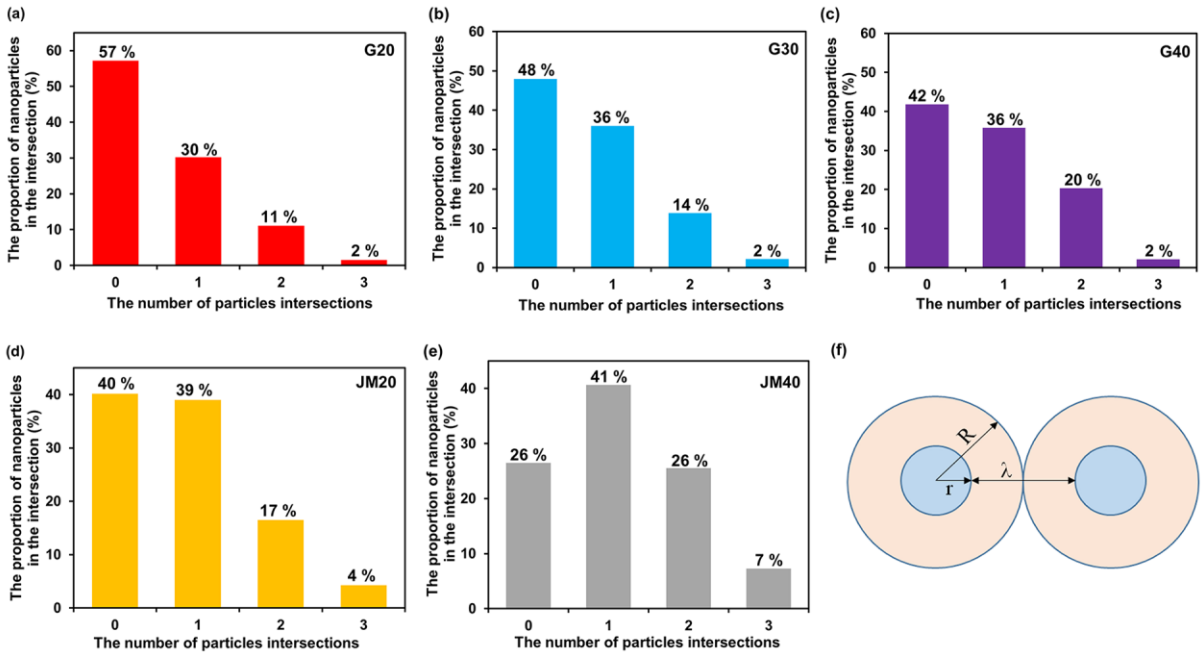

Figure 3: Histograms of the nanoparticles distribution by the number of intersections with "neighbors" (a-e) and a schematic representation of the spherical nanoparticles location within the geometric model (f). See the text below for additional explanations.

In the samples with the measured NPs size, the average distance between the nanoparticles was calculated using a simplified geometric model. It was assumed that spherical particles of the same size are uniformly distributed on the flat surface of the carrier. Within the framework of the model, one can

describe the geometry of NPs distribution having surrounded them with a region of a certain radius R, its value depending on the radius of NPs (r) and the distance between them (λ) (Fig. 3, f).

To determine the values of parameters R and λ, the number of nanoparticles per 1 m^2 of the carbon support was calculated:

$$N_{NP} = \frac{m(Pt)}{m(NP)*S(C)} \qquad (2),$$

where m(Pt) is the mass of platinum applied to 1 g of carbon support,

m(NP) is the mass of one spherical platinum particle (g),

S(C) is the surface area of the carbon support ($m^2\ g^{-1}$), equal to 250 $m^2\ g^{-1}$.

The mass of a spherical particle is determined by its size:

$$m(NP) = \frac{4}{3}\pi r^3 \rho \qquad (3),$$

where ρ is the platinum density ($21.45 * 10^6$ g m^{-3}).

R was calculated according to the formula:

$$R = \frac{0.5}{\sqrt{N(NPs)}} \qquad (4).$$

The average distance between nanoparticles (λ) was calculated by the formula:

$$\lambda = 2(R - r) \qquad (5).$$

The results of the model calculation of the specific number of NPs and the average distance between NPs for the studied catalysts are shown in Table 1.

Characteristics analysis of the platinum NPs spatial distribution carried out in accordance with the results of the TEM micrographs processing (Fig. 2a – e), indicates a greater uniformity of the spatial distribution of platinum NPs in the G series catalysts as compared to the JM20 and JM40 samples. For example, in catalysts G20 and G40, 57% and 42% of NPs, respectively, are not adjacent to their "neighbors". At the same time, in commercial samples JM20 and JM40 of similar composition, the proportion of such NPs is only 40% and 26%, respectively. The share of NPs that has one or more intersections with "neighbors" grows in the series G20 (43%) <G30 (52%) <G40 (58%) ≤JM20 (60%) <JM40 (74%). It is important that, due to the large average size and average mass of NPs in commercial samples, the specific number of such particles is somewhat smaller, and the average distance between

NPs, calculated within the framework of a simplified model, is slightly larger than that for NPs in catalysts G20, G30, and G40 (Table 1). This means that there are no geometric reasons that could cause a lower ordering of NPs spatial distribution on the surface of a carbon support in commercial Pt/C catalysts.

Thus, the original procedure used for the synthesis of Pt/C catalysts made it possible to successfully solve the first of the tasks posed in this study - to obtain Pt/C materials characterized by a smaller size of nanoparticles, their narrower dimensional and more uniform spatial distribution over the surface of the Vulcan XC-72 carbon support, as compared with the commercial electrocatalysts JM20 and JM40.

The cyclic voltammograms of Pt/C catalysts have a characteristic form (Fig. 4). As the content of platinum in the catalysts increases, the specific currents decrease in all sections of the CVs (Fig. 4).

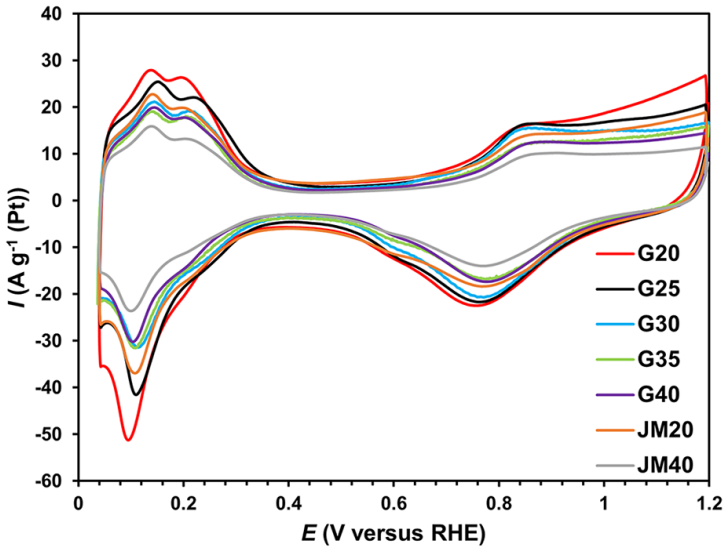

Figure 4: Cyclic voltammograms of Pt/C samples. Sweep rate 20 mV s^{-1}. 2nd cycle. Electrolyte - 0.1 M $HClO_4$ solution saturated with Ar at atmospheric pressure.

The calculation based on the amount of electricity consumed for the electrochemical adsorption and desorption of an atomic hydrogen monolayer showed that an increase in the Pt-loading in the obtained samples (from 20.4 wt.% to 39 wt.%) leads to a decrease in the ESA (from 120 to 88 m^2 g^{-1}(Pt)) (Table 2), which is due to both an increase in the average size and an increase in NPs coalescence (Table 1, Fig. 3).

Table 2: Parameters characterizing electrochemical behavior of Pt/C catalysts

Sample	ESA, m^2 g^{-1}(Pt)	$E_{1/2}$, V (at 1600 rpm)	Number of ē	I_{mass}, A g^{-1}(Pt)	I_{sp}, A m^{-2}(Pt)
G_{20}	120 ± 12	0.92	3.8	250	2.1
G_{25}	116 ± 12	0.93	4.1	220	1.9
G_{30}	98 ± 10	0.92	4.1	208	2.1
G_{35}	93 ± 9	0.92	3.9	194	2.1
G_{40}	88 ± 9	0.94	4.0	186	2.1
JM20	84 ± 8	0.91	3.9	182	2.2
JM40	65 ± 7	0.92	4.0	122	1.9

When comparing the synthesized and commercial catalysts of the same composition, one can see that the ESA of JM catalysts is lower than G (Table 2), which is due to the difference in their structural characteristics described above (Table 1). The commercial catalyst JM40 has the minimal ESA value (Table 2).

The study of the ORR kinetics, carried out by the method of linear voltammetry using RDE (Fig. 5), showed that ORR proceeds according to the 4-electronic mechanism on all catalysts (Table 2). The values of the half-wave potential of oxygen electroreduction vary for the studied catalysts in the range from 0.91 V (JM20) to 0.94 V (G40) (Table 2). Note that the values of the specific kinetic currents of all catalysts are very close and amount to 2.05 ± 0.15 A m^{-2} (Pt) (Table 2). This suggests that a change in the size of the nanoparticles in the range from 2.0 to 3.1 nm does not affect the specific activity of platinum in ORR. The key factor, which determines mass activity of the catalysts under these conditions, is the ESA. As the ESA grows in the series G40 <G35 <G30 <G25 <G20, the mass activity of the synthesized catalysts also increases (Table 2). Note that the mass activity of sample G20 is almost 1.5 times higher than that of JM20, a commercial analog with a similar platinum content (Table 2).

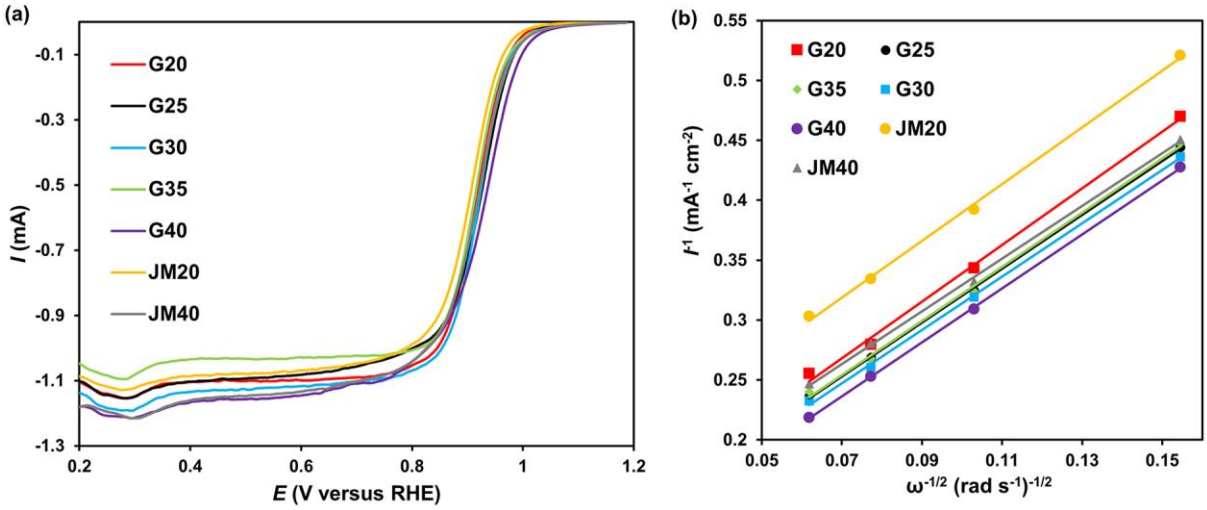

Figure 5: (a) Linear voltammograms of the ORR. The rotation speed of the disk is 1600 rpm^{-1}; (b) j^{-1} - $\omega^{-0.5}$ dependence at 0.90 V potential. The rate of the potential sweep is 20 mV s^{-1}, 0.1 M $HClO_4$ solution saturated O_2 at atmospheric pressure.

During stress testing of the catalysts, a regular decrease in currents occurs which is more pronounced in the oxygen region of the CV (Fig. 6). Interestingly, the value of relative stability of the G series catalysts was found to be the same, independent of either the mass fraction of platinum in the catalysts or the average NPs size (Table 3). Despite the larger size of platinum nanoparticles in commercial catalysts, their relative stability turned out to be somewhat lower than that in the samples we synthesized. Apparently, the higher ordering of the catalyst structure compensates for the negative effect of the smaller NP size on the process of their degradation. According to [14, 34], the decrease in ESA and the activity of catalysts during the cycling of the potential in the range of 0.6 - 1.0 V is largely due to the processes of platinum reprecipitation and coalescence of NPs.

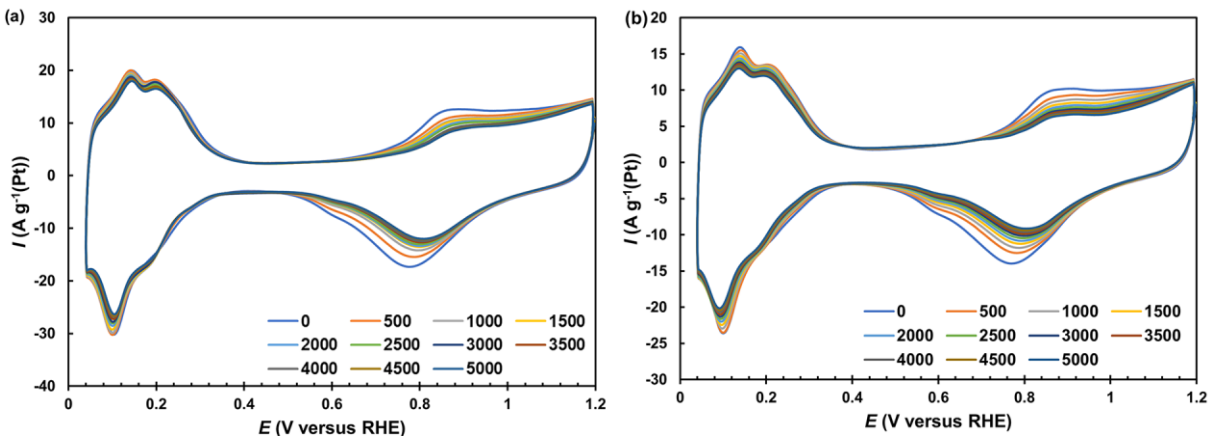

Figure 6: Cyclic voltammograms of (a) G40 and (b) JM40 catalysts measured at a potential sweep rate of 20 mV s^{-1} for every 500 stress test cycles. Electrolyte is 0.1 M $HClO_4$, Ar atmosphere.

It is obvious that the proximity of the NP sizes and the uniformity of their distribution should slow down the course of these negative phenomena. As we have already noted, the positive role of proximity of the NP sizes located in adjacent regions of the catalyst with regard to its stability was demonstrated in [42].

On completion of the stress test, a decrease is observed in the specific activity of the catalysts in ORR, which is most pronounced for samples with a low platinum loading - JM20 and G20. This follows from the comparison of voltammograms (Fig. 7), the values of the specific kinetic currents of ORR on the studied catalysts before (Table 2) and after (Table 3) the completion of the stress test.

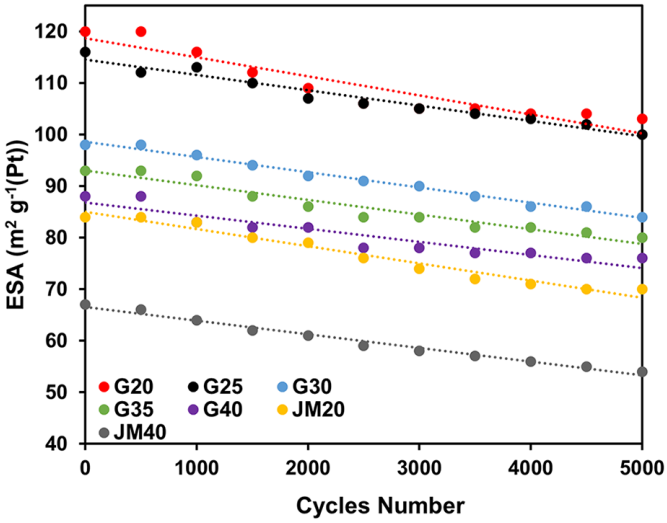

Figure 7: Dependence of the catalysts ESA on the number of stress test cycles.

The relationship between the ORR mass activity of the catalysts with specific activity and ESA can be expressed by the formula [38]:

$$I_{mass} = \sum\left(I_k^{sp}\Theta_k\right)ESA \qquad (6),$$

where I_k^{sp} is the specific activity of the NP surface areas (faces, edges, etc.) of the k-type, Θ_k is the fraction of the nanoparticle surface belonging to the k-type areas. Taking into account platinum nanoparticles with the different number of catalytically active sites on their surface (different types of faces, edges, vertices, steps, etc.), it can be assumed that the smaller the amount of platinum is

contained in the catalytic layer, the faster the proportion of the most active sites decreases during stress testing of the catalysts. Since platinum NPs in samples G20 - G40 have a similar size, and the number of NPs in the catalytic layer increases with an increase in the platinum loading in the catalyst during the test, a much larger amount of oxygen is reduced in catalyst G20 at each NP than in catalyst G40.

Table 3: Parameters characterizing the behavior of electrocatalysts on completion of the stress test

Sample	ESA_{5000}, $m^2\ g^{-1}$	ESA_{5000}/ESA_0, %	Number ē	Electric current at E=0.90 V		$E_{1/2}$, V	$I^{5000}_{mass}/I^{0}_{mass}$, %
				I_{mass}, A g^{-1}(Pt)	I_{Sp}, A m^{-2}(Pt)		
G_{20}	103	86	3.9	118	1.2	0.89	47
G_{25}	100	86	3.8	132	1.3	0.91	60
G_{30}	84	86	3.7	155	1.8	0.92	75
G_{35}	80	86	3.5	145	1.8	0.92	75
G_{40}	76	86	4.2	130	1.7	0.93	70
JM20	69	82	4.3	60	0.9	0.88	33
JM40	55	82	3.6	83	1.5	0.90	69

As a result, reorganization of the NPs structure, accompanied by a decrease in the proportion of the most catalytically active faces, is more pronounced with G20 catalyst than G40 catalyst. At the same time, the total surface area of NPs does not change very much because of the structural reorganization (Tables 2 and 3), which one can see when CVs in their “hydrogen” region before and after the stress test are compared (Fig. 7). This determines proximity of the relative stability values, calculated from the ESA ratio. Another reason for the platinum loading **effect** (the number of NPs in the catalytic layer) on the change in the catalysts activity may be the poisoning of active centers by impurities contained in the solution and in the carbon support. Prior to measurements, identical amount (about 0.036 mg) of each catalyst was applied to the end of the disk electrode (see Experimental section). Taking into account the Pt-loading in the catalysts and the corresponding ESA values (Tables 1 and 2), it is easy to

calculate that the ESA in the initially formed catalytic layers was approximately 8.8 cm^2 for G20 and 12.4 cm^2 for G40. Obviously, with the identical quantity of impurities contained in the solution, the poisoning of the active centers should be more pronounced on catalyst G20, because it is here that a more significant decrease in the ORR specific activity is observed.

On completion of stress testing, the ORR mass activity of the catalysts increases in the following order: JM20<JM40<G20<G40≤G25 <G35<G30 (Table 3). The change in the form of voltammograms before and after stress testing is clearly shown in Figure S4. A decrease in the value of $E_{1/2}$ is observed for all materials, but it is more pronounced for samples G20 and JM20, and less pronounced for - G30, G35, G40 (Fig. S4, Table 3).

Due to the changes in the structural characteristics of the catalysts, values of all three parameters in equation (6) can change in a different way during stress tests of each sample. This may be the reason for some change of the catalysts location in the row of increased mass activity, as compared to their location in the same row before stress tests. Nevertheless, on completion of the stress test, all of the studied G series catalysts remained more active in the ORR compared to the commercial JM20 and JM40 catalysts.

The change in the ESA absolute values during stress testing, shown in Fig. 7 is described by the linear dependence (see the correlation coefficients in Table 4). In the series of catalysts G20 - G40, the rate of ESA reduction, calculated by the tangent of the slope formed by the straight lines, decreases with an increase in the Pt-loading in the materials (Table 4). In this case, values of the ESA rate decrease are very close in catalysts with identical Pt-loading - G20 and JM20; G40 and GM40, respectively (Table 4). However, since the initial ESA for catalysts G20 and G40 are significantly higher than that of JM20 and JM40, the synthesized catalysts G20 and G40 demonstrate higher mass activity on completion of the stress test than their commercial analogs JM20 and JM40.

Table 4: Coefficients of the slope angle formed by the straight-line dependencies "ESA - cycles number" and the correlation parameters of the linear dependence equation

Sample	ω(Pt), wt.%	-k*10^6, m^2	Correlation coefficient, R^2
G_{20}	20.4	3691	0.882
G_{25}	24.6	2982	0.959
G_{30}	30.9	2945	0.987
G_{35}	34.0	2855	0.938
G_{40}	39.0	2545	0.888
JM20	20.0	3327	0.968
JM40	40.0	2655	0.984

Conclusion

Pt/C catalysts G20, G25, G30, G35, G40 containing from 20 to 39 wt% platinum with NPs of a small size (from 2 to 2.6 nm), which demonstrated narrow and uniform size and spatial distribution on the surface and in the pores of the carbon support Vulcan XC-72, were obtained by the liquid phase synthesis.

Due to the smaller size and higher ordering of the NPs spatial distribution, G series catalysts are characterized by higher ESA values (from 120 to 88 m^2 g^{-1}(Pt)) than commercial Pt/C catalysts JM20 and JM40 (Johnson Matthey) (84 and 67 m^2 g^{-1}(Pt)), which contained 20 and 40 wt.% platinum, respectively. The ORR specific activity of all Pt/C catalysts turned out to be approximately the same; however, due to the higher ESA values, the mass activity of G20 and G40 significantly exceeded the mass activity of the corresponding commercial samples JM20 and JM40.

Catalysts degradation was studied with the help of a stress test protocol, used in the "soft" mode, in which voltammetric potential sweep cycles were performed in the range 0.6 - 1.0 V. It was shown that the ESA decrease of catalysts during 5000 stress test cycles is fairly well described by a linear regression equation. The rate of ESA decrease reduces, as the Pt-loading in the catalysts increases; however, it is almost identical for the synthesized and commercial catalysts with similar Pt-loading - G20 and JM20, G40 and JM40, respectively. After stress testing, the catalysts mass activity decreases

less than the ESA. Apparently, the degradation of catalysts is due not only to a decrease in the ESA, but also to a decrease in the fraction of the nanocrystals surface, which belong to the regions with the highest catalytic activity. At the same time, the mass activity of the G series catalysts exceeds the mass activity of commercial analogs both before and after stress testing.

The results of this study show that Pt/C catalysts containing smaller nanoparticles can significantly exceed the catalysts based on larger nanoparticles in terms of ORR mass activity, and they are not inferior to them in stability. The reason for an unexpectedly high stability of catalysts containing small nanoparticles is most likely in the ordering of their structure, which manifests itself in the proximity of the nanoparticle sizes and uniformity of their distribution over the support surface. We have to admit that various methods for synthesizing Pt/C can also have an effect upon the surface of the carbon support and the strength of the platinum NPs adhesion to its surface. Thus, the positive effects of the structural ordering can compensate for the size effect that has a negative influence on NPs stability.

It is important to note that at a similar degradation rate (ESA decrease during the stress test) the Pt/C catalysts, that we have synthesized, demonstrated ORR mass activity which exceeded mass activity of commercial Pt/C analogs by about 30-60%, both in the initial state and on completion of the stress test.

Experimental

Materials

The synthesis of Pt/C catalysts was carried out in the liquid phase according to the procedure described in detail in [16]. Formaldehyde was used as a reducing agent; synthesis was carried out in an atmosphere of carbon monoxide (II). To obtain materials with different mass fractions of platinum, the mass of the carbon support (Vulcan XC-72) was changed, initially having been added to the reaction medium. The composition of the obtained catalysts is given in Table 1.

Commercial Pt/C catalysts JM20 and JM40 (HiSPEC3000, 20 wt.% Pt; HiSPEC4000, 40 wt.% Pt, Johnson Matthey) were used as reference samples.

Methods for certifying the composition and structure of Pt/C materials

The Pt-loading in the studied samples was determined by the gravimetry method. Ceramic crucibles were calcined to get constant weight at 800–850 °C, next they weighed after complete cooling. Then, ~ 0.02 g of Pt/C material was placed in crucibles and kept in a muffle furnace at 800–850 °C for 40 minutes. Crucibles with a non-combustible residue (Pt) were weighed after complete cooling. The difference in weight was used to determine the metal content in the sample.

To study the structural characteristics of the obtained Pt/C materials, we used the powder diffraction method. An ARL X`TRA powder diffractometer with a Bragg-Brentano geometry (θ-θ), CuKα radiation (λ = 0.154056 nm) at room temperature, was used to record X-ray diffraction patterns. X-ray diffraction patterns of the samples under study were recorded in the range of angles $5 \leq 2\theta \leq 90$ degrees by the step-by-step scanning method with a detector movement step of 0.02 degree. The X-ray diffraction patterns were processed with SciDavis software to properly extract the parameters of the peaks, this being of particular significance when they overlapped in the case of the small size particles. The average platinum crystallite size D_{Av} was calculated using the Scherrer equation, as described in more detail in Supporting materials.

The size of platinum nanoparticles, the features of their size and spatial distributions were also studied by transmission electron microscopy (TEM). TEM photographs were obtained using a JEOL JEM F200 microscope (voltage 200 kV, current 12-15 μA, CFEG). To prepare a sample for measurements, 0.5 mg of the catalyst was placed in 1 ml of isopropanol and dispersed by the ultrasound for 10 minutes. A drop of the resulting suspension was applied to a standard copper mesh with a diameter of 3.05 mm, covered with a layer of amorphous carbon 5-6 nm thick, next the sample was dried in air at room temperature for 60 minutes. The histograms of the platinum nanoparticles size distribution in the catalysts were plotted due to results of determining the sizes of at least 400 randomly selected particles in the TEM images in different regions of the sample.

Electrochemical investigation

Electrochemical measurements were performed in a three-electrode cell on a VersaSTAT3 potentiostat using a rotating disk electrode (RDE) (Pine Research Instruments, USA). Saturated silver chloride electrode was used as a reference electrode. The potentials are given with regard to a reversible hydrogen electrode (RHE).

A thin, porous catalyst layer was applied to the electrode using the so-called "catalytic ink". To obtain a suspension of Pt/C catalysts ("catalytic ink"), 900 μl of isopropyl alcohol and 100 μl of a 0.5% aqueous emulsion of Nafion® polymer were added to 6 mg of each sample. Then the suspension was dispersed with the ultrasound for 15 minutes. Under continuous stirring, an aliquot of "ink" 6 μL in volume was taken with a microdispenser and applied to the end of a polished and degreased glassy carbon disk with an area of 0.196 cm^2, the exact weight of the drop being recorded. The electrode was dried in air for 20 minutes while rotating at 700 rpm.

Prior to measuring the electrochemically active surface area (ESA) of the catalyst, the electrolyte was saturated with argon for 40 minutes. Then, 100 cycles were carried out in the potential range from 0.04 to 1.2 V relative to RHE. Potential sweep speed - 200 mV s^{-1}.

The electrochemically active surface area (ESA) was determined from the cyclic voltammogram by calculating the amount of electricity consumed for desorption (Q_d) and adsorption (Q_{ad}) of atomic hydrogen, as described in more detail in Supporting materials. The voltammogram (CV) recording rate was 20 mV s^{-1}, the potential range was from 0.04 to 1.2 V relative to RHE.

To determine the catalysts ORR activity, the electrolyte was saturated with oxygen for 1 hour, after which a series of voltammograms was measured in the range from 0.12 to 1.19 V with a linear potential sweep at a rate of 20 mV s^{-1} at electrode rotation speeds of 400, 900, 1600, and 2500 rpm. The values of mass (I_{mass}) and specific activity (I_{sp}) were calculated for a potential of 0.90 V (RHE).

The method of multiple voltammetric cycling in the potential range of 0.6–1.0 V (RHE) with a sweep rate of 100 mV s^{-1} was chosen as a method for assessing the degree of electrocatalysts degradation. Cycling was carried out in a 0.1 M $HClO_4$ solution saturated with argon at 25 °C for 5000 cycles. After every 500 cycles, two CVs were recorded at a potential sweep rate of 20 mV s^{-1} in the

potential range from 0.04 V to 1.2 V with respect to RHE to calculate the ESA as described above. Detailed calculation of catalyst stability is given in Supporting materials.

Acknowledgements

The authors are grateful to Mr. Nikulin A.Yu. for assistance in the XRD pattern registration and to the “Shared Use Center "High-Resolution Transmission Electron Microscopy” (SFedU) for conducting the TEM studies.

Funding

This research was financially supported by the Ministry of Science and Higher Education of the Russian Federation (State assignment in the field of scientific activity No 0852-2020-0019).

References

1. Crawley, G. Proton exchange membrane (PEM) fuel cells: opening doors to fuel cell commercialization. *Fuel Cell Today* **2006,** 1–12.

2. O'Hayre, R. P. Fuel cell fundamentals. 2nd ed.; John Wiley & Sons Limited: New York, **2009**.

3. Kongkanand, A.; Mathias, M. F. *J. Phys. Chem. Lett.* **2016**, *7*, 1127–1137. doi: 10.1021/acs.jpclett.6b00216

4. Katsounaros, I.; Cherevko, S.; Zeradjanin, A. R.; Mayrhofer, K. J. J. *Angew. Chem. Int. Ed.* **2014**, *53*, 102–121. doi:10.1002/anie.201306588

5. Chan, S.; Jankovic, J.; Susac, D.; Saha, M. S.; Tam, M.; Yang, H.; Ko, F. *J. Mater. Sci.* **2018**, *53*, 11633–11647. doi:10.1007/s10853-018-2411-4

6. Yaroslavtsev, A. B.; Dobrovolsckiy, Yu. A.; Shaglaeve, N. S.; Frolova, L. A.; Gerasimova, E. V.; Sanginov, E. A. *Russ. Chem. Rev.* **2012**, *81*, 191–201. doi: 10.1070/RC2012v081n03ABEH004290

7. Litster, S.; McLean, G. *J. Power. Sources.* **2004**, *130*, 61–76. doi:10.1016/j.jpowsour.2003.12.055

8. Jung, N.; Chung, D. Y.; Ryu, J.; Yoo, S. J.; Sung, Y-E. *Nano today* **2014**, *9*, 433–456. doi: 10.1016/j.nantod.2014.06.006

9. Borup, R.; Meyers, J.; Pivovar, B.; Kim, Yu.S.; Mukundan, R.; Garland, N.; Myers, D.; Wilson, M. et al. *Chem Rev*. **2007**, *107*, 3904–3951. doi: 10.1021/cr050182l

10. Sheng, S.; Xiaoying, W.; Xintong, Zh.; Yuehong, S.; Saffa, R.; Chang-jun, L. *J. Mater. Chem. A* **2017**, *5*, 1808–1825. doi: 10.1039/C6TA08580F

11. Dai, S.; Zhang, J.; Fu, Y.; Li, W. *J. Mater. Sci*. **2017**, *53*, 423–434. doi:10.1007/s10853-017-1508-5

12. Kinoshit, K. *J. Electrochem. Soc.* **1990,** *137*, 845–848. doi:10.1149/1.2086566

13. Gasteiger, H. A. *Appl. Catal. B Environ.* **2005**, *56*, 9–35. doi:10.1016/j.apcatb.2004.06.021

14. Meier, J. C.; Galeano, C.; Katsounaros, I.; Witte, J.; Bongard, H. J.; Topalov, A. A.; Baldizzone, C.; Mezzavilla, S. et al. *Beilstein J. Nanotechnol.* **2014,** *5*, 44–67. doi: 10.3762/bjnano.5.5

15. Garlyyev, B.; Kratzl, K.; Rück, M.; Michalička, J.; Fichtner, J.; Macak, J.M.; Kratky, T.; Günther, S. et al. *Angew. Chem. In.t Ed.* **2019,** *58*, 9596–9600. doi: 10.1002/anie.201904492

16. Alekseenko, A. A.; Ashihina, E. A.; Shpanko, S. P.; Volochaev, V. A.; Safronenko, O. I.; Guterman, V. E. *Appl. Catal. B Environ.* **2018,** *226*, 608–615. doi: 10.1016/j.apcatb.2018.01.013

17. Rossi, K.; Asara, G. G.; Baletto, F. *ACS Catal.* **2020,** *10*, 3911−3920. doi: 10.1021/acscatal.9b05202

18. Xia, Y.; Zhao, M.; Holder, J.; Chen, Z.; Xie, M.; Cao, Z.; Chi, M. *ChemCatChem* **2019,** *11*, 2458–2463. doi: 10.1002/cctc.201900239

19. Rossi, K.; Asara, G. G.; Baletto, F. *ACS Catal.* **2020,** *10*, 3911−3920. doi: 10.1021/acscatal.9b05202

20. Leontyev, I. N.; Belenov, S. V.; Guterman, V. E.; Haghi-Ashtiani, P.; Shaganov, A. P.; Dkhil, B. *J. Phys. Chem. C* **2011,** *115*, 5429–5434. doi: 10.1021/jp1109477

21. Holby, E. F.; Sheng, W.; Shao-Horn, Y.; Morgan, D. *Energy. Environ. Sci.* **2009,** *2*, 865–871. doi: 10.1039/b821622n

22. Holby, E. F.; Antolini, E.; Salgado, J. R. C.; Gonzalez, E. R. *J. Power Sources* **2006,** *160*, 957–968. doi: 10.1016/j.jpowsour.2006.03.006

23. Cherevko, S.; Kulyk, N.; Mayrhofer, K. J. J. *Nano Energy* **2016**, *29*, 275–298. doi: 10.1016/j.nanoen.2016.03.005

24. Stamenkovic, V. R.; Mun, S. B.; Mayrhofer, K. J. J.; Ross, Ph. N.; Markovic, N. M. *J. Am. Chem. Soc.* **2006**, *128*, 8813–8819. doi: 10.1021/ja0600476

25. Capelo, A.; Esteves, M. A.; Sa, A. I.; Silva, R. A.; Cangueiro, L.; Almeida, A.; Vilar, R.; Rangel, C. M. *Int J Hydrogen Energy* **2016,** *41*, 12962–12975. doi: 10.1016/j.ijhydene.2016.06.127

26. Hasché, F.; Oezaslan, M.; Strasser, P. *Phys. Chem. Chem. Phys.* **2010,** *12*, 15251–15258. doi: 10.1039/C0CP00609B

27. Takeia, C.; Kakinuma, K.; Kawashima, K.; Tashiro, K.; Watanabe, M.; Uchida, M. *J. Power Sources* **2016,** *324*, 729–737. doi: 10.1016/j.jpowsour.2016.05.117

28. Baschuk, J. J.; Li, X. *Int. J. Energy Res.* **2001,** *25*, 695–713. doi: 10.1002/er.713

29. Yan, W-M.; Chu, H-S.; Lu, M-X.; Weng, F-B.; Jung, G-B.; Lee, Ch. *J Power Sources* **2009,** *188*, 141–147. doi: 10.1016/j.jpowsour.2008.11.107

30. Park, Y-C.; Kakinuma, K.; Uchida, M.; Tryk, D. A.; Kamino, T.; Uchida, H.; Watanabe, M. *Electrochem. Acta* **2013,** *91*, 195–207. doi: 10.1016/j.electacta.2012.12.082

31. Shao, Y.; Yin, G.; Gao, Y. *J. Power Sources* **2007,** *171*, 558–566. doi: 10.1016/j.jpowsour.2007.07.004

32. Shao-Horn, Y.; Sheng, W. C.; Chen, S.; Ferreira, P. J. *Top Catal.* **2007,** *46*, 285–305. https://doi.org/10.1007/s11244-007-9000-0

33. Xie, J.; Wood, D. L.; More, K. L.; Atanassov, P.; Borup, R. L. *J Electrochem Soc.* **2005,** *152*, 1011–1020. doi: 10.1149/1.1873492

34. Guterman, V. E.; Belenov, S. V.; Alekseenko, A. A.; Tabachkova, N. Yu.; Volochaev, V. A. *Russ J Electrochem.* **2017**, *53*, 531–539. doi: 10.1134/S1023193517050081

35. Moguchikh, E. A.; Alekseenko, A. A.; Guterman, V. E.; Novikovsky, N. M.; Menshchikov, V. S.; Tabachkova, N. Y. *Russ J Electrochem.* **2018**, *11*, 979–989. doi: 10.1134/S0424857018130376

36. Zhang, Y.; Chen, S.; Wang, Y.; Ding, W.; Wu, R.; Li, L.; Qi, X.; Wei, Z. *J Power Sources* **2015,** *273*, 62–69. doi: 10.1016/j.jpowsour.2014.09.012

37. Cherevko, S.; Kulyk, N.; Mayrhofer, K. J. J. *Nano Energy* **2016,** *29*, 275–298. doi: 10.1016/j.nanoen.2016.03.005

38. Guterman, V. E.; Belenov, S. V.; Alekseenko, A. A.; Rui, L.; Tabachkova, N. Yu.; Safronenko, O. I. *Electrocatal.* **2018,** *9*, 550–562. doi: 10.1007/s12678-017-0451-1

39. Watanabe, M.; Yano, H.; Uchida, H.; Tryk, D. A. *J. Electroanal. Chem.* **2018**, *819*, 359–364. doi:10.1016/j.jelechem.2017.11.017

40. Dendooven, J.; Ramachandran, R. K.; Solano, E.; Kurttepeli, M.; Geerts, L.; Heremans, G.; Ronge, J.; Minjauw, M. M. et al. *Nat. Commun.* **2017,** *8*, 1074. doi: 10.1038/s41467-017-01140-z

41. Yano, H.; Watanabea, M.; Iiyamaa, A.; Uchida, H. *Nano Energy* **2016,** *29*, 323–333. doi: 10.1016/j.nanoen.2016.02.016

42. Alinejad, Sh.; Quinson, J.; Schröder, J.; Kirkensgaard, J. J. K.; Arenz, M. *ACS Catal.* **2020,** *10*, 13040–13049. doi: 10.1021/acscatal.0c03184

43. Favilla, P. C.; Acosta, J. J.; Schvezov, C. E.; Sercovich, D. J.; Collet-Lacoste, J. R. *Chem. Eng. Sci.* **2013,** *101*, 27–34. doi:10.1016/j.ces.2013.05.067

44. Gusev. A. I. Nanomaterials, nanostructures, nanotechnologies. 2nd ed.; Physmathlit: Moscow, **2009**.